Boundary Control of Full-Bridge ZVS: Natural Switching Surface for Transient and Steady-State Operation

Germán G. Oggier, *Member, IEEE*, and Martin Ordonez, *Member, IEEE*

***Abstract*—This paper presents the use of a high-performance boundary controller for the full-bridge zero-voltage-switching topology. An enhanced dynamic response is obtained by employing the natural switching surface (SS), which is thoroughly derived in the normalized geometrical domain. The advantages of the normalization are the simple graphical representation, the generality for any combination of parameters, and the mathematical simplicity. Recently, nonisolated basic topologies have benefited from advancements in boundary control. The analysis and derivation in this work bring the benefit of outstanding dynamic performance to this isolated topology. As demonstrated in this work, the relationship between the leakage and output filter inductances makes the formulation of the natural trajectories for isolated converters possible. The resulting SS provides an excellent dynamic response during start-up, reference change, and sudden output loading conditions. Experimental results are presented to illustrate the characteristics and advantages of the control scheme and the converter operation with fixed switching frequency.**

***Index Terms*—Boundary control, full-bridge (FB) zero-voltage switching (ZVS) (FB-ZVS) converters, isolated dc–dc converters, natural switching surface (SS) (NSS).**

I. Introduction

THE full-bridge (FB) zero-voltage-switching (ZVS) (FB-ZVS) converter is extensively applied in medium- to high-power dc/dc power conversion, becoming a traditional topology employed in a variety of industrial power conversion applications where simplicity along with high efficiency, high power density, high reliability, and low electromagnetic interference is required [1]–[3]. The converter uses ZVS to reduce switching loss, allowing high switching frequency operation and small energy storage components [4], [5].

However, the FB-ZVS converter has critical disadvantages, such as loss of duty cycle due to transformer leakage inductance, reduction of operation range under ZVS, and, also, output voltage overshoot [6]. In order to deal with these weaknesses, several improvements to the topology have been proposed to cover different applications such as computer and telecommunication applications [7], electric vehicle [8], fuel cell [9], and onboard battery charger [10], among others. For example, in [11], a steady-state analysis of the topology is performed to give design guidelines. As a result, tradeoff in selecting the auxiliary circuit components is given to optimize the performance of the overall converter. In [12], a coupled inductor is used to achieve ZVS of the primary switches in the entire line and load range. In [13], three-phase ZVS dc–dc converter is proposed where high efficiency at half power load can be obtained. Other solutions have included extra passive circuits to extend the ZVS range and also to reduce the output voltage overshoot [6], [14]–[16].

Fast dynamic response of this topology is an important requirement to meet the particular specifications for each application. For this particular topology, the literature discusses classic small-signal modeling techniques [17]–[19]. A small-signal model applied to FB-ZVS converter is presented in [20], where it is shown that the small-signal dynamics of the control to output transfer function using voltage-mode control does not exhibit a second-order pole due the output $L-C$ filter, like the basic buck converter. There is a characteristic pole dependent of the switching frequency, leakage inductor, and output inductor values, which is independent of operating conditions.

All previous techniques have been unable to predict the large-signal behavior of the converter, as it is shown in [21]. An improvement is obtained if current mode control is used, as is proposed in [22], where a current mode control phase-shifted pulsewidth-modulation converter is derived based on the current sampling model of current mode control and main characteristics such as output impedance, audiosusceptibility, and control to output transfer function are obtained. It can be shown that, by using current mode control, the need for additional zero in the compensation network of the error amplifier is eliminated. Furthermore, current mode control provides an effective way to avoid saturation of the magnetic core of the high-frequency transformer.

Classic controllers have been conceived for linear time-invariant systems, and since power converters present nonlinear behavior, linear approximations are required in order to apply this theory to them [23]. Although the small-signal analysis theory provides a framework for the analysis and design of linear controllers, the dynamic response is not satisfactory in many cases, establishing the need for other nonlinear control

Manuscript received October 31, 2012; revised January 24, 2013; accepted March 2, 2013. Date of publication March 19, 2013; date of current version August 9, 2013.

G. G. Oggier is with the Consejo Nacional de Investigaciones Científicas y Técnicas, Buenos Aires, Argentina, and also with the Grupo de Electrónica Aplicada (GEA), Facultad de Ingenieria, Universidad Nacional de Rio Cuarto, Rio Cuarto X5804BYA, Argentina (e-mail: goggier@ieee.org).

M. Ordonez is with the Department of Electrical and Computer Engineering, The University of British Columbia, Vancouver, BC V6T 1Z4, Canada (e-mail: mordonez@ieee.org).

Color versions of one or more of the figures in this paper are available online at http://ieeexplore.ieee.org.

Digital Object Identifier 10.1109/TIE.2013.2253076

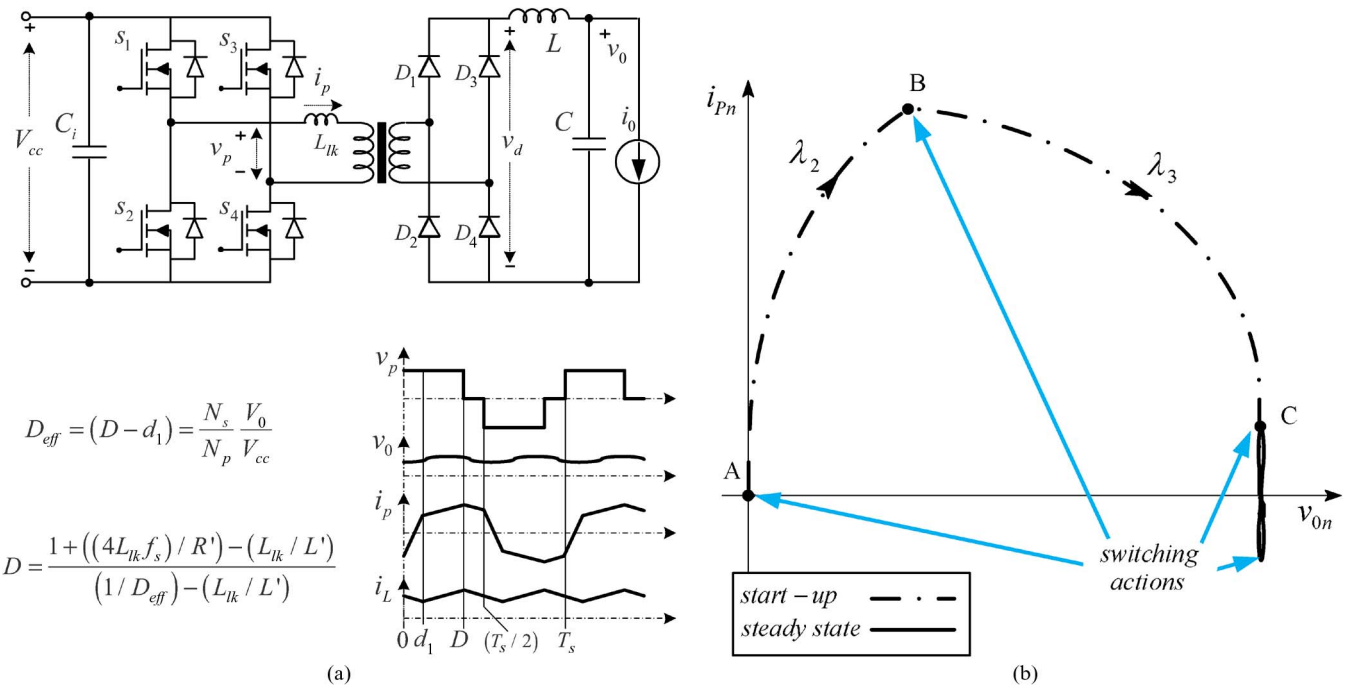

Fig. 1. (a) FB-ZVS converter topology, main theoretical waveforms, and steady-state relationships for voltage gain and primary duty cycle [18] and (b) control law concept for the FB-ZVS converter using the NSS corresponding to start-up condition.

schemes to improve the transient behavior. For example, in [24], a nonlinear current programming technique for FB-ZVS converters is presented, where the output voltage and capacitor current are sensing, in order to estimate the output voltage to obtain the gate signals. Another technique based on boundary control or geometric control has been gaining attention in the last decades [25], [26]. By using boundary control with curved switching surface (SS), it is possible to provide good robustness and good dynamic response for the converter and to guarantee that there will be no overshoot during transients. In particular, the natural SS (NSS), which is a novel control method based on curved SSs, was implemented for basic dc–dc topologies, buck-derived inverters, and power factor corrections, accomplishing superior transient characteristics [27]–[30].

This paper explores the use of natural trajectories for isolated converters and applies the theory to the FB-ZVS. As a result of employing the NSS, unprecedented dynamic response is achieved for start-up, reference, and load change transients. This remarkable feature is demonstrated with simulation and experimental results in this paper and presents a technique to avoid transformer saturation under any operating condition. Furthermore, fixed-frequency operation is one of the features of the proposed strategy. Results illustrate the benefits of the proposed control strategy for operation during start-up and load transient operation.

This paper is the complete version of a preliminary conference paper [31]. In this enhanced version of the paper, a complete set of simulation and experimental results are included to validate and illustrate the performance of the proposed controller. As well, the analysis of the operation of the converter in steady state and design expressions to operate the converter with constant switching frequency are included, along with the details of the implementation.

II. FB-ZVS Topology and Normalized Derivation

The FB-ZVS topology main waveforms and steady-state relationships are shown in Fig. 1(a). It consists of an FB working as a dc–ac converter feeding a high-frequency transformer, which supplies a rectifier connected to an output LC filter [18]. The analysis of the FB-ZVS converter could be simplified by referring the model to one side of the transformer and considering its magnetizing inductance to be much larger than its leakage inductance. Therefore, the branch with the magnetizing inductance may be considered as an open circuit. For the present analysis, the transformer turns ratio will be considered hereinafter equal to one, and the output voltage is controlled via phase shifting. Both legs of the FB operate with a 50% duty cycle, and the phase difference between the voltage generated by each leg is controlled. The phase difference can be $0 < \phi < 1$ and assumes the role of the duty cycle D in this converter in a similar way to the basic structures [17]. Fig. 1(b) shows a conceptual representation of the FB-ZVS converter using the NSS during start-up, where the solid lines correspond to steady-state operation and dashed lines correspond to a start-up transient condition.

Fig. 2 shows the different structures of the FB-ZVS topology according to the state of the power switches, where solid line indicates the active circuit and dashed line indicates the passive circuit. The different structures are defined as follows: structure I for $v_{L_{lk}} = V_{cc}$ and $v_L = -v_0$, structure II for $(v_{L_{lk}} + v_L) = V_{cc} - v_0$, structure III for $(v_{L_{lk}} + v_L) = -v_0$, structure IV for $v_{L_{lk}} = -V_{cc}$ and $v_L = -v_0$, structure V for $(v_{L_{lk}} - v_L) = -V_{cc} + v_0$, and structure VI for $(v_{L_{lk}} - v_L) = v_0$. It is important to note that transitions from structure I to structure II are realized in a natural way when i_p equals the value of i_L referred to the primary of the transformer, whereas transitions from structure II to structure III are realized when a switching action occurs. Similar situation occurs for second half cycle.

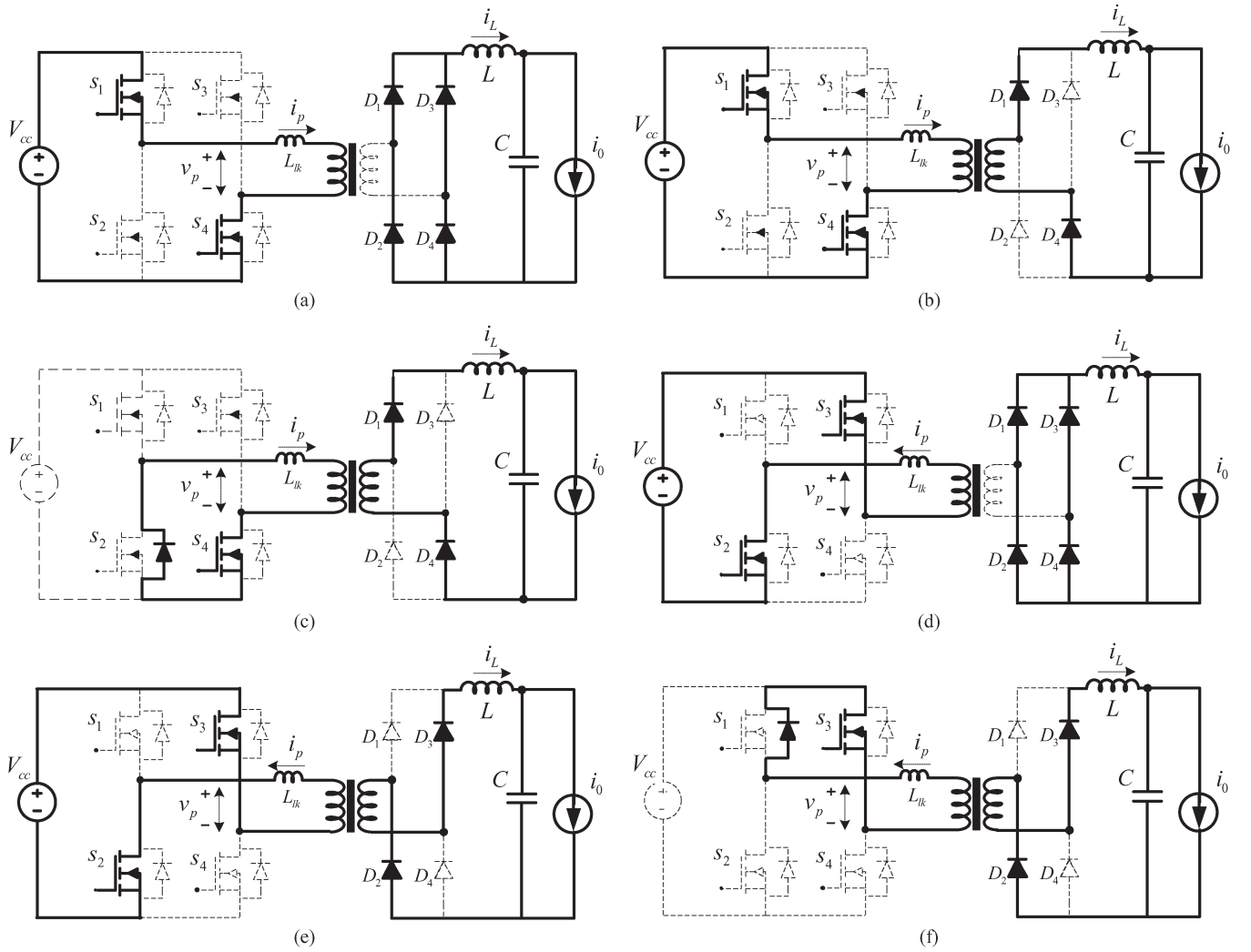

Fig. 2. FB-ZVS converter structures: (a) $v_{L_{lk}} = V_{cc}$ and $v_L = -v_0$; (b) $(v_{L_{lk}} + v_L) = V_{cc} - v_0$; (c) $(v_{L_{lk}} + v_L) = -v_0$; (d) $v_{L_{lk}} = -V_{cc}$ and $v_L = -v_0$; (e) $(v_{L_{lk}} - v_L) = -V_{cc} + v_0$; (f) $(v_{L_{lk}} - v_L) = v_0$.

Fig. 2 shows the different structures of the converter according to the state of the power switches. These structures correspond to waveforms shown in Fig. 1(a) in steady state as follows: Structure I is valid when $0 < t \leq d_1 T_s$, structure II is valid when $d_1 T_s < t \leq DT_s$, and structure III is valid when $DT_s < t \leq T_s/2$. Similar conditions can be expressed for the second half-period.

A constant current load was selected since it has infinite impedance and can represent both a large loading condition and no damping effect simultaneously. This operating condition translates into the worst case scenario in terms of stability.

The derivation of the natural trajectories is presented to cover the different modes of operation of the converter. Considering the first half cycle, the model of the converter can be represented with a system of differential equations as follows.

For structure I [see Fig. 2(a)],

$$\frac{di_p}{dt} = \frac{1}{L_{lk}}(V_{cc}) \tag{1}$$

$$\frac{di_L}{dt} = \frac{1}{L}(-v_0) \tag{2}$$

$$\frac{dv_0}{dt} = \frac{1}{C}(i_L - i_0). \tag{3}$$

For structure II [see Fig. 2(b)],

$$i_p = i_L \tag{4}$$

$$\frac{di_L}{dt} = \frac{1}{(L + L_{tk})}(V_{cc} - v_0) \tag{5}$$

$$\frac{dv_0}{dt} = \frac{1}{C}(i_L - i_0). \tag{6}$$

Finally, for structure III [see Fig. 2(c)],

$$i_p = i_L \tag{7}$$

$$\frac{di_L}{dt} = \frac{1}{(L + L_{lk})}(-v_0) \tag{8}$$

$$\frac{dv_0}{dt} = \frac{1}{C}(i_L - i_0). \tag{9}$$

In order to simplify the mathematical representation of the converter, a normalization technique is employed to disengage some of the parameters of the converter. The normalization is performed by using the characteristic impedance of the combined L and C values, $Z_0 = \sqrt{L/C}$, natural frequency

TABLE I
NATURAL TRAJECTORIES OF THE FB-ZVS CONVERTER

$$\lambda_1 = v_{0n} - \cos\left(\frac{k\,(i_{pn} - i_{Ln,\lambda_1})}{V_{ccn}}\right) + (i_{Ln,\lambda_1} + i_{on})\sin\left(\frac{k\,(i_{pn} - i_{Ln,\lambda_1})}{V_{ccn}}\right)$$

$$\lambda_2 = (V_{ccn} - v_{0n})^2 - (i_{Ln,\lambda_2} - i_{on})^2 - \frac{(V_{ccn}-1)^2}{(1+k)} + (i_{Ln} - i_{0n})^2$$

$$\lambda_3 = (-v_{0n})^2 - (i_{Ln,\lambda_3} - i_{on})^2 - \frac{1}{(1+k)} + (i_{Ln} - i_{0n})^2$$

$f_0 = 1/T_0 = 1/(2\pi\sqrt{LC})$, and the converter reference voltage V_r as base quantities as follows:

$$v_{xn} = \frac{v_x}{V_r} \tag{10}$$

$$i_{xn} = \frac{i_x}{V_r} Z_0 \tag{11}$$

$$t_n = t.f_0 \tag{12}$$

where v_x and i_x represent generic voltages and currents and v_{xn} and i_{xn} represent their respective normalized values.

After applying normalization and solving the differential equation, the solution to structure I [(1)–(3)] can be written as

$$i_{pn} = \frac{2\pi}{k} V_{ccn} t_n + i_{pn}(0) \tag{13}$$

$$i_{Ln} = (i_{Ln}(0) - i_{0n})\cos(2\pi t_n) - v_{0n}(0)\sin(2\pi t_n) + i_{0n} \tag{14}$$

$$v_{0n} = (i_{Ln}(0) - i_{0n})\sin(2\pi t_n) + v_{0n}(0)\sin(2\pi t_n) \tag{15}$$

where k is the relationship between leakage inductance and the output filter inductor.

The solution for structures II and III associated to expressions (4)–(9) can be written as

$$i_{Ln} = (i_{Ln}(0) - i_{0n})\cos\left(\frac{2\pi t_n}{\sqrt{(1+k)}}\right) - \frac{(v_{0n}(0) - V_{ccn})}{\sqrt{(1+k)}}\sin\left(\frac{2\pi t_n}{\sqrt{(1+k)}}\right) + i_{0n} \tag{16}$$

$$v_{0n} = \sqrt{(1+k)}\,(i_{Ln}(0) - i_{0n})\sin\left(\frac{2\pi t_n}{\sqrt{(1+k)}}\right) + (v_{0n}(0) - V_{ccn})\cos\left(\frac{2\pi t_n}{\sqrt{(1+k)}}\right) + V_{ccn} \tag{17}$$

and

$$i_{Ln} = (i_{Ln}(0) - i_{0n})\cos\left(\frac{2\pi t_n}{\sqrt{(1+k)}}\right) - \frac{(v_{0n}(0))}{\sqrt{(1+k)}}\sin\left(\frac{2\pi t_n}{\sqrt{(1+k)}}\right) + i_{0n} \tag{18}$$

$$v_{0n} = \sqrt{(1+k)}\,(i_{Ln}(0) - i_{0n})\sin\left(\frac{2\pi t_n}{\sqrt{(1+k)}}\right) + (v_{0n}(0))\cos\left(\frac{2\pi t_n}{\sqrt{(1+k)}}\right) \tag{19}$$

respectively.

By using trigonometric identities and performing a transformation process, time can be eliminated from (13)–(19) yielding the expressions λ_1, λ_2, and λ_3 shown in Table I for the normalized natural trajectories of the FB-ZVS converter in the first half cycle. The expressions of λ_4, λ_5, and λ_6 are deduced similarly. Terms i_{Ln,λ_1}, i_{Ln,λ_2}, and i_{Ln,λ_3}, shown in Table I, are derived in order to operate the converter under constant switching frequency.

Fig. 3(a) shows the normalized natural trajectories of the converter previously derived, in the i_{pn}-versus-v_{0n} plane. Normalized natural trajectories λ_2 and λ_3 (λ_5 and λ_6) are circles with center in (V_{cc}, i_0) and $(0, i_0)$, respectively, whereas natural trajectories λ_1 and λ_4 can be considered as straight lines in the region of interest. In order to show the effects of changing the values of L and L_{lk}, Fig. 3(b) shows natural trajectories in the i_p-versus-v_0 plane.

As can be deduced from Fig. 3(a), when the structure corresponding to trajectory λ_2 is active and the output voltage is lower than the reference, the output voltage will increase until trajectory λ_3 is reached. For example, λ_2 is part of the start-up. On the other hand, if trajectory λ_3 is active and the output voltage is higher than the reference, the output voltage will decrease until trajectory λ_4 is reached. Finally, trajectories λ_1 and λ_4 are the responsible for the change of polarity of the primary transformer current i_p from positive to negative and vice versa, respectively.

Trajectory λ_1 is present only when the circles corresponding to trajectories λ_2 and λ_6 (λ_3 and λ_5) are not matched, as occurs in steady state. It corresponds to the structure shown in Fig. 2(a). It starts when the power switches S_1 and S_4 are turned on and finalizes when i_p current becomes equals to the reflected output inductor current. Trajectory λ_2 corresponds to the structure shown in Fig. 2(b), and it is present when the same power switches S_1 and S_4 are turned on and the i_p current is higher than the reflected output inductor current. Finally, trajectory λ_3 corresponds to the structure shown in Fig. 2(c), and it is present when the power switches S_2 and S_4 are turned on. A similar explanation is valid for the second half cycle.

III. CONTROL LAW

The behavior of the converter using the natural trajectories can be synthesized in a simple conceptual definition and with the aid of Fig. 3. The objective of the control law is to maintain the operating point around the reference output voltage in

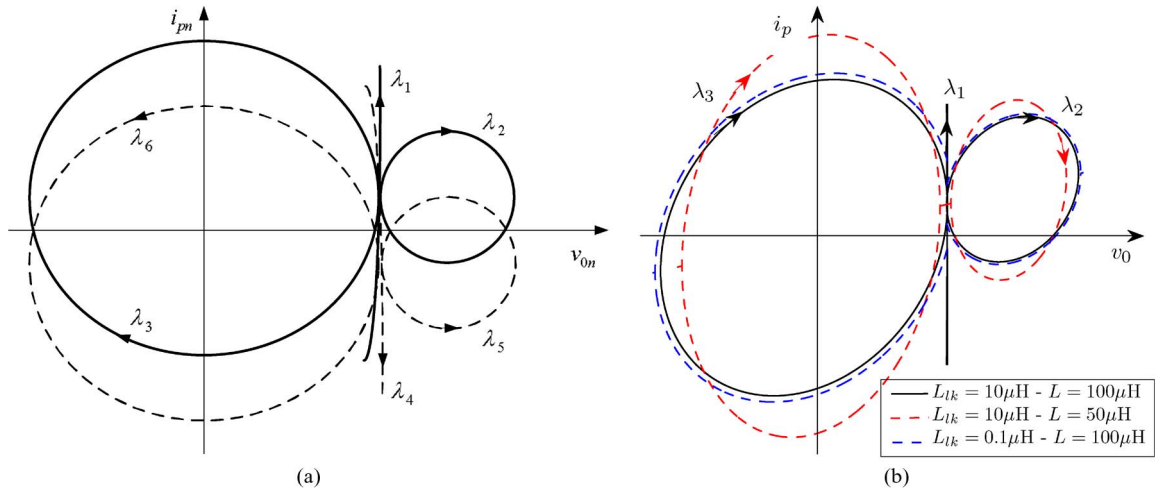

Fig. 3. (a) Normalized natural trajectories for the ZVS converter and (b) effect of the changes of the leakage inductance and output filter inductor on the SS.

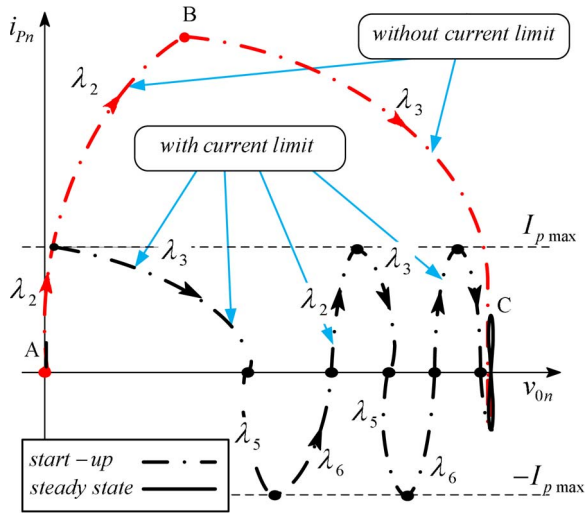

Fig. 4. Conceptual trajectories by using the NSS during an start-up for two situations: (a) Without maximum current limit and (b) with maximum current limit.

steady state by switching between the different natural trajectories. In order to keep a balance of the transformer current, the next sequence has to be satisfied in a full switching period: $\lambda_1 \rightarrow \lambda_2 \rightarrow \lambda_3 \rightarrow \lambda_4 \rightarrow \lambda_5 \rightarrow \lambda_6$.

Note that transitions $\lambda_1 \rightarrow \lambda_2$ and $\lambda_4 \rightarrow \lambda_5$ are natural, and these are not controlled by a switching action.

Let us define $u_1 = 1$ when S_1 is turned on and S_2 is turned off and $u_1 = 0$ when S_1 is turned off and S_2 is turned on. Similarly, $u_2 = 1$ when S_3 is turned on and S_4 is turned off and $u_2 = 0$ when S_3 is turned off and S_4 is turned on. Thus, the primary voltage of the transformer v_p can be expressed as $v_p = V_{cc}$ when $u_1 = 1$ and $u_2 = 0$; $v_p = 0$ when $u_1 = 1$ and $u_2 = 1$ or $u_1 = 0$ and $u_2 = 0$; and $v_p = -V_{cc}$ when $u_1 = 0$ and $u_2 = 1$.

Fig. 4 illustrates conceptually a start-up operation. The control law forces the following condition: The converter starts at point A with the state $u_1 = 1$ and $u_2 = 0$ and moves along the normalized inductor current axis until the surface λ_2 is reached at point B. When this SS is reached, the control law switches to state $u_1 = 1$ and $u_2 = 1$ upwards to arrive at point C, followed by a change of the state of the switches to $u_1 = 0$ and $u_2 = 1$. This state continues to achieve the steady-state surface. Once the steady-state surface is reached, the control law follows the sequence to ensure that the operating point follows the output voltage reference. Both the output voltage and the transformer current are considered as varying references to establish the control law.

Fig. 4 also shows the normalized phase plane when a maximum current limit mode is used. Using this mode, the maximum inductor current is limited to $\pm I_{p\ \max}$. The SS are chosen in order to reach the steady-state condition after a few switching cycles, which are functions of the value of the $I_{p\ \max}$ imposed by the semiconductor devices and the transformer magnetizing level. By limiting the current, the control law maintains the voltage balance of the transformer to avoid saturation during transients.

When a voltage reference or load change occurs, the operating point is located outside of the plane delimited by the intersection of the steady-state natural trajectories producing either negative or positive values of the corresponding natural trajectories. Then, the control law follows the switching sequence in order to reach the boundary of the plane that determines steady-state operation with a minimum number of switching actions. Thereafter, a change in the structure of the system is performed to force the operating point to follow the perimeter of the plane. Fig. 5 also shows different transient conditions when output voltage reference change to an upper and lower value in dashed lines.

In [25] and [26], it is demonstrated that the operating points along the SS can be classified into three different categories by analyzing λ_x and $d\lambda_x/dt$ as follows: 1) Reflective points have trajectories on both sides directed toward it ($\lambda_x > 0$ and $d\lambda_x/dt < 0$ and $\lambda_x < 0$ and $d\lambda_x/dt > 0$), which results in sliding mode behavior; 2) rejective points have trajectories on both sides directed away from it ($\lambda_x < 0$ and $d\lambda_x/dt < 0$ and $\lambda_x > 0$ and $d\lambda_x/dt > 0$), making the converter unstable; and 3) refractive points have one trajectory directed toward it, and the other one away from it ($d\lambda_x$ has the same sign on both sides).

By evaluating the derivative of the SSs, it can be concluded that, in one side, the trajectory is directed toward the SS and,

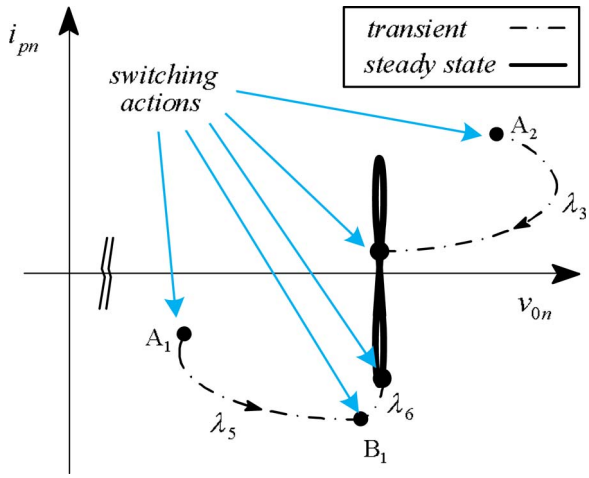

Fig. 5. Phase plane corresponding to large-signal transient operation.

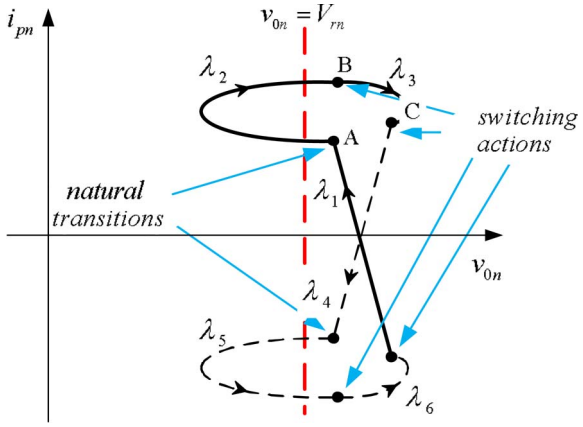

Fig. 6. Phase plane corresponding to steady-state operation.

on the other side, $d\lambda_x/dt = 0$, i.e., the trajectory is tangential to the SS, and then the converter will operate in the boundary between reflective and refractive operation. This demonstrates that the operation of the converter with the proposed control law will be stable.

IV. Steady-State Operation

In this section, the FB-ZVS converter steady-state operation is explained, and the expressions of i_{Ln,λ_x} to operate the converter with constant switching frequency are derived. The value of i_{Ln,λ_x} based on the steady-state operation of the converter should be evaluated carefully, as it could vary significantly with the operating point and also according to the natural trajectory.

Fig. 6 shows the phase plane between i_{pn} and v_{0n} variables when the converter operates in steady state. The surface corresponds with the intersection of natural trajectories defined in the previous section. In this figure are also indicated the different structure defined in Fig. 2. From this figure, it can be observed that, in steady state, the output voltage is continuously changing around the reference output voltage and the average primary current is equal to zero. This is a mandatory condition in order to avoid the saturation of the high-frequency transformer.

The normalized transformer currents i_{pnA}, i_{pnB}, and i_{pnC} shown in Fig. 6 correspond to normalized currents $i_p(0)$, $i_p(d_1)$, and $i_p(D)$, respectively, as it is shown in Fig. 1(a).

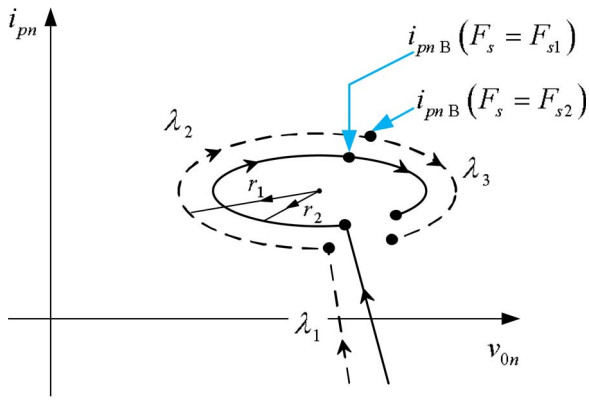

Fig. 7. Phase plane for two different reference switching frequencies.

Table II presents these current expressions and demonstrates their dependence on the switching frequency.

A. Operation With Constant Switching Frequency

As can be deduced from the equations given in Table I, the values of i_{Ln,λ_x} modify the radius of the circles corresponding to natural trajectories λ_2 and λ_3 (λ_5 and λ_6). Thus, selecting the values of i_{Ln,λ_x}, in order to modify the radius of the circles shown in Fig. 3(a) so that normalized current values correspond to the natural trajectories, will ensure that the converter would operate with the desired switching frequency. Fig. 7 shows the phase plane for two different reference switching frequency concepts.

Thus, the initial condition of the transformer currents can be evaluated using the steady-state current expression at the switching angles given in Table II, setting $T_s = 1/F_s^*$, where F_s^* is the desired switching frequency.

By applying normalization, the following expressions can be obtained

$$i_{pnA} = \left(\frac{i_p(0)|_{T_s=1/F_s^*} Z_0}{V_r}\right) \tag{20}$$

$$i_{pnB} = \left(\frac{i_p(d_1)|_{T_s=1/F_s^*} Z_0}{V_r}\right) \tag{21}$$

$$i_{pnC} = \left(\frac{i_p(D)|_{T_s=1/F_s^*} Z_0}{V_r}\right). \tag{22}$$

Replacing (20)–(22) in expressions given in Table I, i_{Ln,λ_1}, i_{Ln,λ_2}, and i_{Ln,λ_3} can be solved.

The mechanism to prevent saturation in steady-state operation is achieved by means of controlling trajectories II and IV. Fig. 8 shows conceptually a modification of trajectory II to adjust the current set point when a positive dc transformer current component is present. Dashed lines in the time-domain plot display the effect on the duty cycle of the primary voltage waveform that results from changing the equivalent radius of the natural trajectory in the geometrical domain.

V. Results

Simulation and experimental results of a ZVS FB converter are presented in this section to verify the behavior of the NSS. Table III presents the converter specifications, and Fig. 9 shows a block diagram of the experimental setup. The NSS control

TABLE II
EXPRESSIONS OF i_p AT THE SWITCHING ANGLES IN STEADY STATE

$$i_p(0) = -\frac{V_0(4V_{cc}L - V_{cc}RT_s + RT_sV_0)(V_{cc}L + V_{cc}L_{lk} + L_{lk}V_0)}{4RV_{cc}(V_{cc}L - L_{lk}V_0)(L + L_{lk})}$$

$$i_p(d_1) = \frac{V_0(4V_{cc}L - V_{cc}RT_s + RT_sV_0)(V_{cc}L + V_{cc}L_{lk} - L_{lk}V_0)}{4RV_{cc}(V_{cc}L - L_{lk}V_0)(L + L_{lk})}$$

$$i_p(D) = \frac{V_0\left[\left(4L^2 - L_{lk}RT_s + 4L_{lk}L + RT_sL\right)V_{cc}{}^2 + (-V_0RT_sL - 4V_0L_{lk}L)V_{cc} + RT_sL_{lk}V_0{}^2\right]}{4RV_{cc}(V_{cc}L - L_{lk}V_0)(L + L_{lk})}$$

where $R = V_0/I_0$, $T_s = 1/F_s$ and F_s is the switching frequency in steady state.

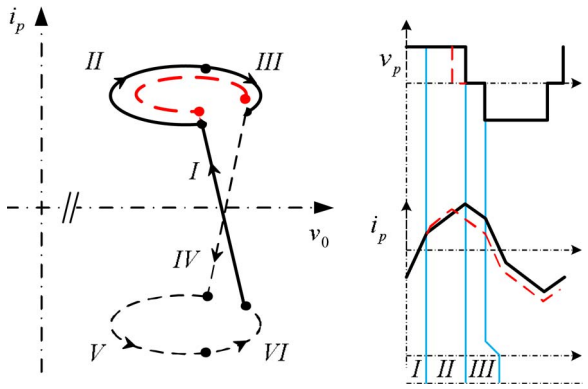

Fig. 8. Conceptual transformer voltage-second change with trajectory II.

TABLE III
EXPERIMENTAL PROTOTYPE CHARACTERISTICS

Maximum output power ($P_{0\,\max}$)	500 W
Switching frequency (f_S)	20 kHz
Transformer turns ratio (n)	1/2.5
Leakage inductance (L_{lk})	1 μH
Output filter inductance (L)	100 μH
Output capacitor (C)	20 μF
Maximum inductor current	50 A

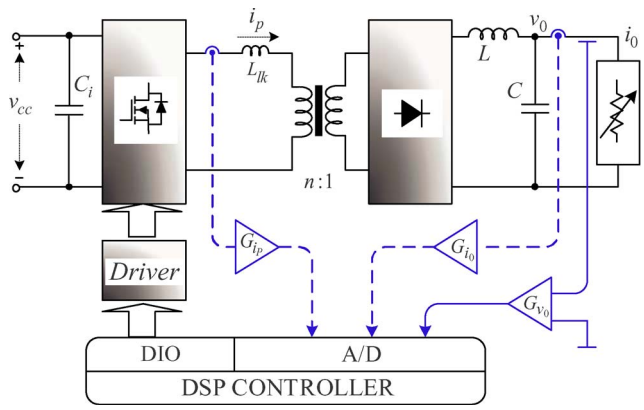

Fig. 9. Block diagram of the experimental setup.

laws were implemented using a TMS320F2812 fixed-point DSP.

The parameters of the converter were chosen with the main objective of enhancing the visualization of the results and showing clearly how the control law works with the different transient situations, in particular the phase plane representation.

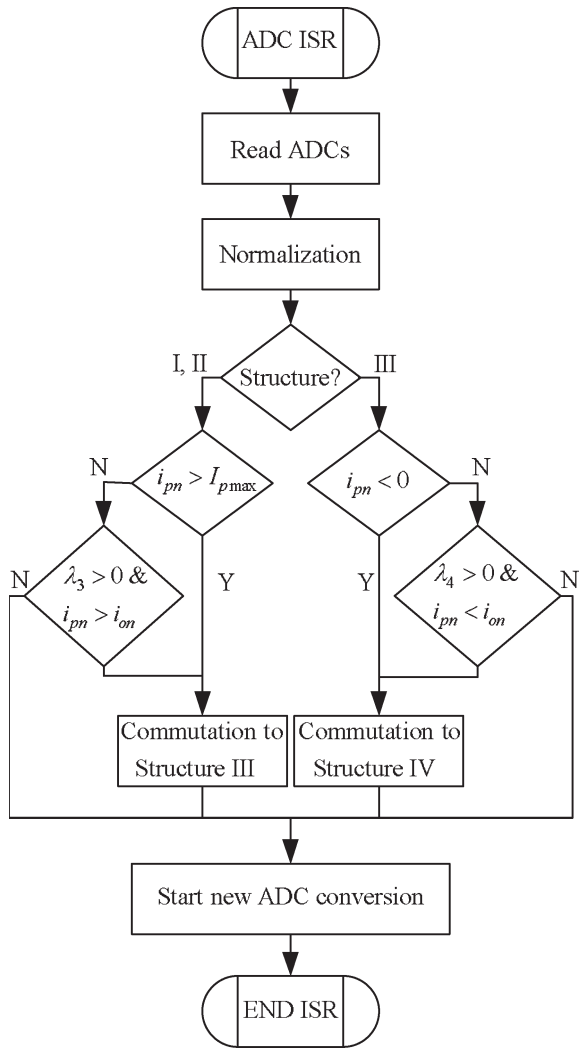

Fig. 10. DSP control algorithm flowchart.

The controller is implemented with a DSP, and the processing power of the digital core defines how fast the algorithm can be computed and, therefore, the maximum switching frequency of the converter. With the ongoing price reductions of high-performance DSP processors, the controller can be implemented at a reasonable cost.

Fig. 10 shows the sequence of actions in the analog-to-digital converter interrupting routine considering the first half cycle, which is called every time that the conversion of all the measured variables is completed.

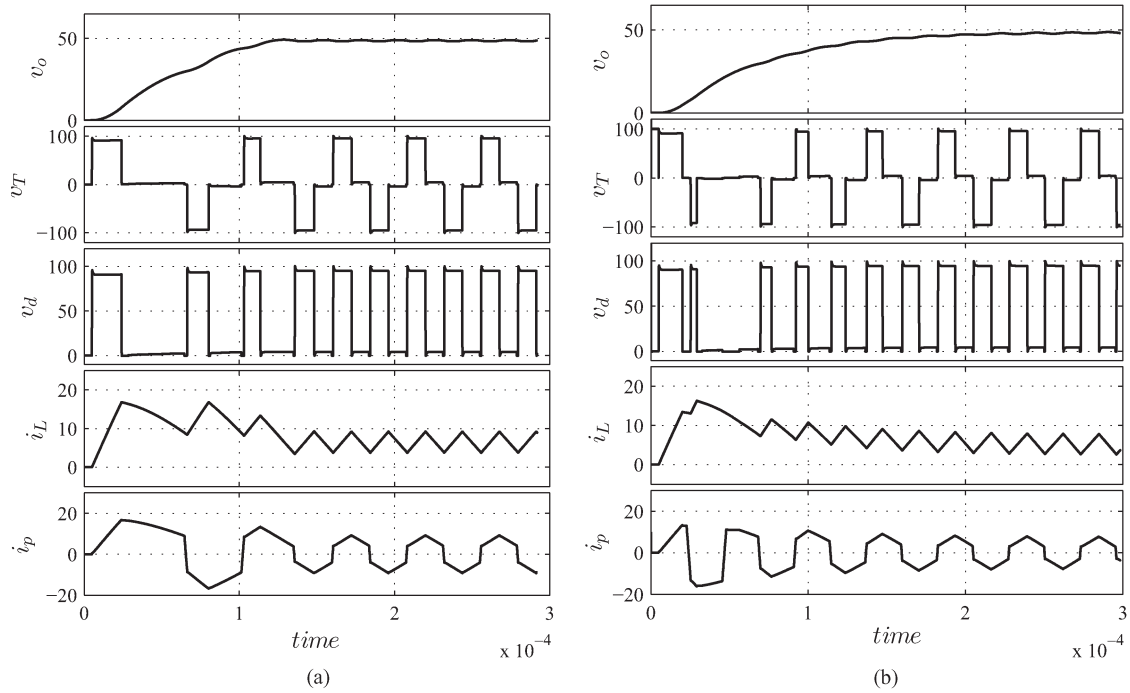

Fig. 11. Start-up simulation results for the FB-ZVS converter: (a) By using the NSS and (b) by using a PID classical controller.

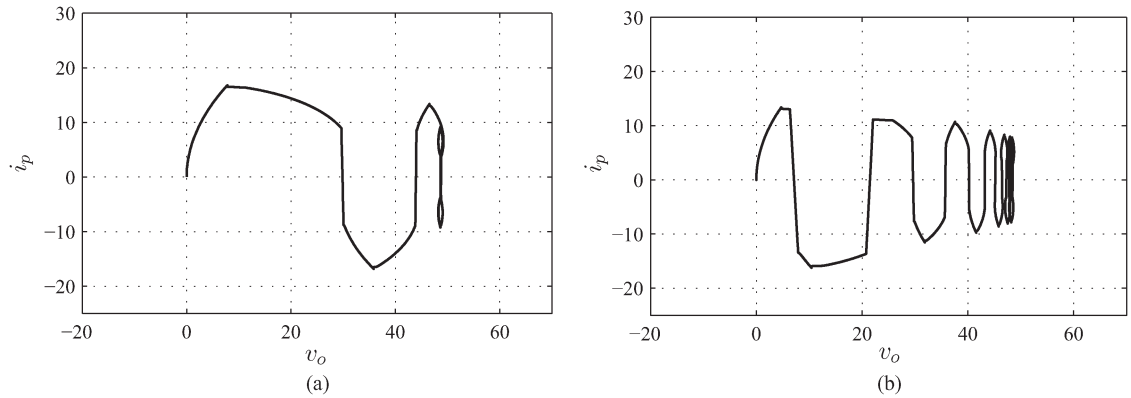

Fig. 12. Phase plane trajectories during the start-up: (a) By using the NSS and (b) by using a PID classical controller.

A. Simulation Results

The start-up condition takes the output voltage from 0 V to the nominal output voltage of 50 V. The obtained start-up transient simulation result is shown in Fig. 11(a) with a control of maximum current of 18 A. During this transient, the control law follows the sequence explained in Section III (Fig. 4) from time zero until steady state is reached. These results are compared to those obtained with a classical linear controller using a PID compensator. The simulation results are shown in Fig. 11(b).

It can be observed that the maximum current of the power switches is the same for both control strategies, but the transient response using the NSS is better than the response obtained using a linear controller. The system reaches steady state after 0.2 ms when using a linear controller compared to 0.12 ms obtained using the NSS.

Fig. 12(a) and (b) shows the state plane trajectories during the start-up cases described previously. When the NSS is used, the target is accomplished in a few switching actions, while if a linear controller is used, it takes many transitions to reach the target. From these results, it can be observed that, by using the NSS, the maximum current is met two times during the transient, resulting in a faster start-up response and allowing a more efficient use of power switches.

Fig. 13 shows the simulated dynamic response of the converter for two cases: a sudden load change from 5 to 10 A (a) and a change of reference from 50 to 70 V for the FB-ZVS converter using the NSS (b). Both results show that the target operating point is reached in one switching action. It is worth noting that the dynamic behavior using a resistive load is comparable to that of constant current load case. Fig. 14(a) and (b) shows the state plane trajectories during a change of load and change of reference, respectively. In Fig 14(a), it can be observed that a change of load causes the natural surface to experience changes in the center and in the radius of the corresponding circles of λ_2 and λ_3. Fig. 14(b) shows how the control law choose the structures in order to reach the target in one switching actions.

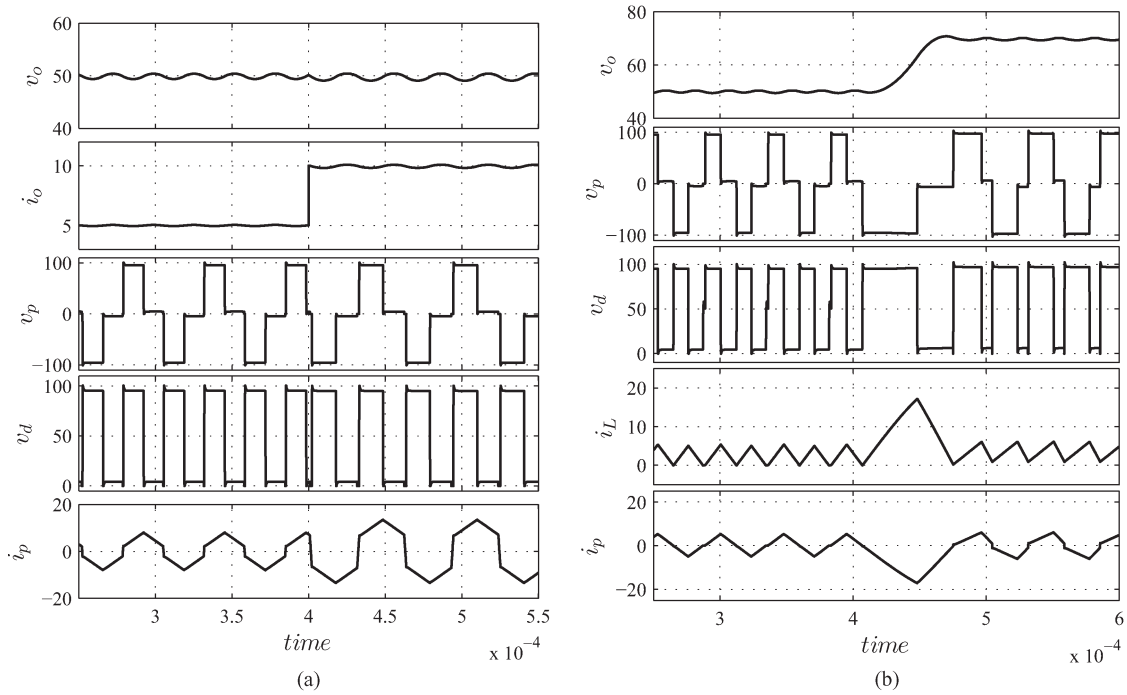

Fig. 13. (a) Change of load simulation results from 5 to 10 A and (b) change of reference simulation results from 50 to 70 V for the FB-ZVS converter using the NSS.

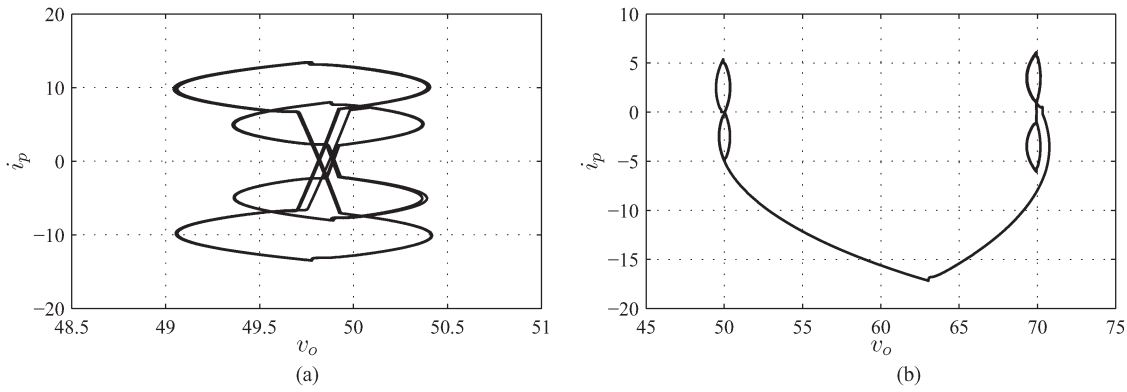

Fig. 14. (a) Phase plane trajectories for change of load from 5 to 10 A and (b) phase plane trajectories for change of reference from 50 to 70 V for the FB-ZVS converter using the NSS.

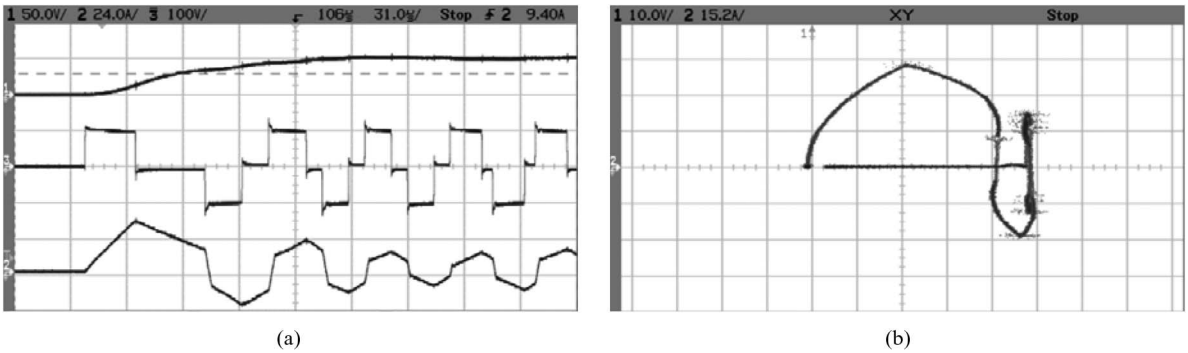

Fig. 15. Start-up experimental results for the FB-ZVS converter using the NSS. (a) Transient response: Output voltage (Ch1), primary transformer current (Ch2), and primary transformer voltage (Ch4). (b) State plane trajectories: Output voltage (Ch1) and primary current (Ch2).

B. Experimental Results

Fig. 15 shows the experimental results during start-up transient from 0 to 50 V when the maximum current limit mode is active: Fig. 15(a) shows transient response, and Fig. 15(b) shows the state plane. Since the experimental prototype includes a high-frequency transformer, the control law switching

Fig. 16. Output voltage reference change experimental results for the FB-ZVS converter using the NSS from 50 to 70 V: Output voltage (Ch1), primary transformer voltage (Ch3), and primary transformer current (Ch2).

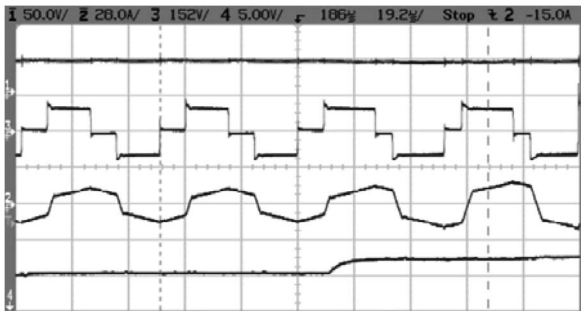

Fig. 17. Load change experimental results for the FB-ZVS converter using the NSS from 5 to 8 A: Output voltage (Ch1), primary transformer voltage (Ch3), primary transformer current (Ch2), and output current (Ch4).

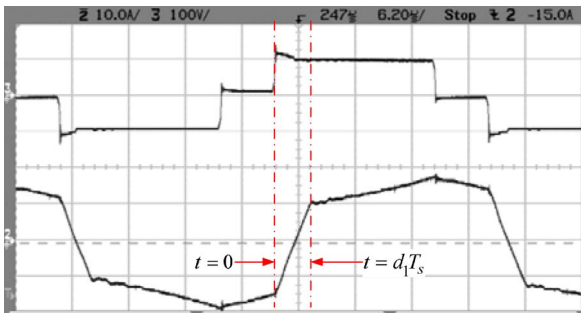

Fig. 18. Steady-state experimental results for the FB-ZVS converter: Primary transformer voltage (Ch3) and primary transformer current (Ch2).

sequence successfully prevented saturation of the magnetic core as was explained in Section IV.

Fig. 16 shows the experimental dynamic response for an output voltage reference change from 50 to 70 V, and Fig. 17 shows the experimental dynamic response when a sudden change of load from 5 to 8 A occurs. It can be observed that the experimental results are in close agreement with the simulation results.

Fig. 18 shows the operation of the converter and confirms its operation under ZVS condition through the inspection of the primary transformer current and voltage. It can be observed that the primary transformer current is negative when time equals zero and positive when time equals $d_1 T_s$, therefore meeting the requirement for ZVS operation [18].

VI. Conclusion

A curved SS for control of the FB-ZVS converters has been presented in this paper. The SS was derived in the normalized domain to provide generality to the analysis. Under this control scheme, the converter showed an excellent dynamic behavior, with no overshoot and time-optimal response for start-up and load disturbances, achieving steady state in only one switching action. In addition to the enhanced dynamic response, fixed-frequency operation was realized using the steady-state information. Finally, a prototype was implemented using the calculated parameters to test the NSS, confirming the enhanced characteristics of the proposed technique.

References

[1] S. Yong-Saeng, K. Chang-Seop, and H. Sang-Kyoo, "A pulse-frequency-modulated full-bridge DC/DC converter with series boost capacitor," *IEEE Trans. Ind. Electron.*, vol. 58, no. 11, pp. 5154–5162, Nov. 2011.

[2] L. Palma and P. N. Enjeti, "A modular fuel cell, modular DC–DC converter concept for high performance and enhanced reliability," *IEEE Trans. Power Electron.*, vol. 24, no. 6, pp. 1437–1443, Jun. 2009.

[3] A. J. Mason, D. J. Tschirhart, and P. K. Jain, "New ZVS phase shift modulated full-bridge converter topologies with adaptive energy storage for SOFC application," *IEEE Trans. Power Electron.*, vol. 23, no. 1, pp. 332–342, Jan. 2008.

[4] F. Liu, J. Yan, and X. Ruan, "Zero-voltage and zero-current-switching PWM combined three-level DC/DC converter," *IEEE Trans. Ind. Electron.*, vol. 57, no. 5, pp. 1644–1654, May 2010.

[5] H.-K. Yoon, S.-K. Han, E. Choi, G. Moon, and M. Youn, "Zero-voltage switching and soft-commutating two-transformer full-bridge PWM converter using the voltage-ripple," *IEEE Trans. Ind. Electron.*, vol. 55, no. 3, pp. 1478–1488, Mar. 2008.

[6] U. Prasanna and A. Rathore, "Extended range ZVS active-clamped current-fed full-bridge isolated DC/DC converter for fuel cell applications: Analysis, design and experimental results," *IEEE Trans. Ind. Electron.*, vol. 60, no. 7, pp. 2661–2672, Jul. 2013.

[7] B. Lin, J. Dong, and J. Chen, "Analysis and implementation of a ZVS/ZCS DC–DC switching converter with voltage step-up," *IEEE Trans. Ind. Electron.*, vol. 58, no. 7, pp. 2962–2971, Jul. 2011.

[8] M. Pahlevaninezhad, P. Das, J. Drobnik, P. Jain, and A. Bakhshai, "A novel ZVZCS full-bridge DC/DC converter used for electric vehicles," *IEEE Trans. Power Electron.*, vol. 27, no. 6, pp. 2752–2769, Jun. 2012.

[9] M. Ordonez and J. E. Quaicoe, "Soft-switching techniques for efficiency gains in full-bridge fuel cell power conversion," *IEEE Trans. Power Electron.*, vol. 26, no. 2, pp. 482–492, Feb. 2011.

[10] T. Kim, S. Lee, and W. Choi, "Design and control of the phase shift full bridge converter for the on-board battery charger of the electric forklift," in *Proc. IEEE ICPE-ECCE Asia*, 2011, pp. 2709–2716.

[11] P. K. Jain, W. Kang, H. Soin, and Y. Xi, "Analysis and design considerations of a load and line independent zero voltage switching full bridge DC/DC converter topology," *IEEE Trans. Power Electron.*, vol. 17, no. 5, pp. 649–657, Sep. 2002.

[12] Y. Jang, M. M. Jovanovic, and Y.-M. Chang, "A new ZVS-PWM full-bridge converter," *IEEE Trans. Power Electron.*, vol. 18, no. 5, pp. 1122–1129, Sep. 2003.

[13] J. Aguillon-Garcia and M. Gun-Woo, "A high-efficiency three-phase ZVS PWM converter utilizing a positive doubles-star active rectifier stage for server power supply," *IEEE Trans. Ind. Electron.*, vol. 58, no. 8, pp. 3317–3329, Aug. 2011.

[14] I. Lee and G. Moon, "Analysis and design of phase-shifted dual H-bridge converter with a wide ZVS range and reduced output filter," *IEEE Trans. Ind. Electron.*, vol. 60, no. 10, pp. 4415–4426, Oct. 2013.

[15] D. V. Ghodke, K. Chatterjee, and B. G. Fernandes, "Modified soft-switched three-phase three-level DC–DC converter for high-power applications having extended duty cycle range," *IEEE Trans. Ind. Electron.*, vol. 59, no. 9, pp. 3362–3372, Sep. 2012.

[16] M. Pahlevaninezhad, J. Drobnik, P. K. Jain, and A. Bakhshai, "A load adaptive control approach for a zero-voltage-switching DC/DC converter used for electric vehicles," *IEEE Trans. Ind. Electron.*, vol. 59, no. 2, pp. 920–933, Feb. 2012.

[17] R. W. Erickson and D. Maksimovic, *Fundamentals of Power Electronics*, 2nd ed. Secaucus, NJ, USA: Kluwer, 2001, ch. 7.
[18] J. A. Sabate, V. Vlatkovic, R. B. Ridley, F. C. Lee, and B. H. Cho, "Design considerations for high-voltage high-power full-bridge zero-voltage-switching PWM converter," in *Proc. IEEE APEC*, 1990, pp. 275–284.
[19] S. M. khazraei, A. Rahmati, and A. Abrishamifar, "Small signal and large signal charge control models for a phase-shifted PWM converter," in *Proc. IEEE ICIT*, 2008, pp. 1–6.
[20] M. J. Schutten and D. A. Torrey, "Improved small-signal analysis for the phase-shifted PWM power converter," *IEEE Trans. Power Electron.*, vol. 18, no. 2, pp. 659–669, Mar. 2003.
[21] V. Vlatkovic and J. A. Sebate, "Small-signal analysis of the phase-shifted PWM converter," *IEEE Trans. Power Electron.*, vol. 7, no. 1, pp. 128–135, Jan. 1992.
[22] X. Xiaofeng, "Small-signal model for current mode control full-bridge phase-shifted ZVS converter," in *Proc. IEEE IPEM Conf.*, 2000, pp. 514–518.
[23] P. F. Kocybik and K. N. Bateson, "Digital control of a ZVS full-bridge DC–DC converter," in *Proc. IEEE 10th Annu. APEC*, 1995, pp. 687–693.
[24] V. Sui-pung Cheung and H. Shu-hung Chung, "Capacitor current programming technique for phase-shift DC–DC converter," in *Proc. IEEE ECCE*, 2011, pp. 1251–1258.
[25] R. Munzert and P. T. Krein, "Issues in boundary control," in *Proc. IEEE PESC*, 1996, pp. 810–816.
[26] M. Greuel, R. Muyshondt, and P. T. Krein, "Design approaches to boundary controllers," in *Proc. IEEE PESC*, 1997, pp. 672–678.
[27] M. Ordonez, M. T. Iqbal, and J. E. Quaicoe, "Selection of a curved switching surface for buck converters," *IEEE Trans. Power Electron.*, vol. 21, no. 4, pp. 1148–1153, Jul. 2006.
[28] J. M. Galvez, M. Ordonez, F. Luchino, and J. E. Quaicoe, "Improvements in boundary control of boost converters using the natural switching surface," *IEEE Trans. Power Electron.*, vol. 26, no. 11, pp. 3367–3376, Nov. 2011.
[29] M. Ordonez, J. E. Quaicoe, and M. T. Iqbal, "Advanced boundary control of inverters using the natural switching surface: Normalized geometrical derivation," *IEEE Trans. Power Electron.*, vol. 23, no. 6, pp. 2915–2930, Nov. 2008.
[30] J. M. Galvez and M. Ordonez, "High performance boundary control of boost-derived PFCs: Natural switching surface derivation and properties," *IEEE Trans. Power Electron.*, vol. 27, no. 8, pp. 3807–3816, Aug. 2012.
[31] G. G. Oggier and M. Ordonez, "Boundary control for isolated topologies—The natural switching surface for full-bridge ZVS," in *Proc. IEEE ECCE*, 2012, pp. 3981–3987.

Germán G. Oggier (M'10) was born in Córdoba, Argentina. He received the Electr. Eng. degree and the M.Sc. degree in electrical engineering from the Universidad Nacional de Rio Cuarto, Rio Cuarto, Argentina, in 2003 and 2006, respectively, and the Dr. degree in control systems from the Universidad Nacional del Sur, Argentina, in 2009.

During 2011–2012, he was a Postdoctoral Fellow with Simon Fraser University, Metro Vancouver, BC, Canada. His postdoctoral research activities were in the area of boundary control of power converters. He is currently a Lecturer in the Grupo de Electrónica Aplicada, Universidad Nacional de Rio Cuarto. He is also a Researcher with the Consejo Nacional de Investigaciones Cientificas y Técnicas, Buenos Aires, Argentina. His current research interests include power electronics, electric vehicles, and renewable energy conversion.

Martin Ordonez (S'02–M'09) was born in Neuquen, Argentina. He received the Ing. degree in electronic engineering from the National Technological University, Buenos Aires, Argentina, in 2003 and the M.Eng. and Ph.D. degrees in electrical engineering from the Memorial University of Newfoundland, St. John's, NL, Canada, in 2006 and 2009, respectively.

He is an Assistant Professor with the Department of Electrical and Computer Engineering, The University of British Columbia, Vancouver, BC, Canada. He is also an Adjunct Professor with Simon Fraser University, Burnaby, BC, and Memorial University of Newfoundland. His industrial experience in power conversion includes research and development (R&D) with Xantrex Technology Inc./Elgar Electronics Corporation (currently, AMETEK Programmable Power), Deep-Ing Electronica de Potencia, and TRV Dispositivos, where he developed high-density dc–dc power converters, UPS inverters, and digital controllers. He has an active research program in power conversion for renewable energy systems and has developed partnerships with various companies in the sector. With the support of industrial funds and the Natural Sciences and Engineering Research Council, he contributed to more than 50 publications and R&D reports in the power area.

Dr. Ordonez was awarded with the David Dunsiger Award for excellence in the Faculty of Engineering and Applied Science (2009), the Chancellor's Graduate Award/Birks Graduate Medal, and as a Fellow of the School of Graduate, Memorial University.